

Prediction of room-temperature two-dimensional π -electron half-metallic ferrimagnets

J. Phillips,¹ J. C. G. Henriques,^{1,2} J. Fernández-Rossier,^{1,*} and A. T. Costa^{3,1}

¹*International Iberian Nanotechnology Laboratory (INL),
Av. Mestre José Veiga, 4715-330 Braga, Portugal*[†]

²*Universidade de Santiago de Compostela, 15782 Santiago de Compostela, Spain*

³*Department of Physics, Center of Physics (CF-UM-UP),
University of Minho, Campus of Gualtar, 4710-057, Braga, Portugal*

(Dated: April 17, 2026)

We propose a strategy to obtain conducting organic materials with fully spin-polarized Fermi surface, lying at a singular flat band, with antiferromagnetically coupled magnetic moments that reside in pi-orbitals of nanographenes. We consider a honeycomb crystal whose unit cell combines two different molecules with $S = 1/2$: an Aza-3-Triangulene, a molecule with orbital degeneracy, and a 2-Triangulene. The analyzed system is half-metallic with a ferrimagnetic order, presenting a zero net total magnetic moment per unit cell. We combine density functional theory calculations with a Hubbard model Hamiltonian to compute the magnetic interactions, the bands, the intrinsic Anomalous Hall effect, and the collective spin excitations. We obtain very large intermolecular exchange couplings, in the range of 50 meV, which ensures room temperature stability. When the magnetization is off-plane, intrinsic spin orbit coupling in graphene opens up a topological gap that, despite being very small, leads to a quantized Hall conductance in the tens of mK range. Above 1 Kelvin, the system will behave like a half-metal with fully compensated magnetic moments, thereby combining two characteristics that make it ideal for spintronics applications.

The search for materials exhibiting spin-split electronic bands and vanishing net magnetization is an extremely active area of research[1–4]. Spin splitting is a key figure of merit for many spintronic applications, including tunnel magnetoresistance[5–7]. In conventional spintronic devices, spin polarization is typically provided by ferromagnetic layers; however, these generate stray magnetic fields that couple to other circuit elements and are detrimental for sensing and memory applications. In this context, altermagnetic spintronics has recently emerged as a particularly active field, as altermagnets exhibit spin-split bands along specific crystallographic directions while maintaining zero net magnetization[8, 9].

Half-metallic fully compensated ferrimagnets[10–13] constitute another class of materials sharing several of the properties that make altermagnets fundamentally appealing. These systems display complete spin polarization of the electronic states together with zero total magnetization. The magnetic moments of the distinct sublattices are antiparallel and cancel macroscopically, while the electronic structure remains half-metallic, with a band gap in one spin channel and metallic behavior in the other. This combination enables fully spin-polarized charge transport in the absence of stray magnetic fields, distinguishing these materials from conventional ferromagnetic half-metals. As a result, half-metallic fully compensated ferrimagnets are of strong fundamental interest for elucidating the interplay between electronic structure and magnetic order and are highly attractive for spintronic applications[14, 15].

Here, we propose a route to engineering half-metallic fully compensated ferrimagnetism in triangulene crystals. Triangulenes are a prototypical class of open-shell nanographene structures that serve as experimentally re-

alizable building blocks for constructing larger molecular architectures with tailored magnetic properties[16–32]. Advances in on-surface synthesis and ultra-high-vacuum experimental techniques [33–35] have enabled the fabrication of triangulenes with different sizes[17, 22, 36–38], as well as dimers[19], rings[24, 25], chains[24], and two-dimensional lattices[39, 40].

Our starting point is the recent observation that non-centrosymmetric triangulene crystals, with a unit cell composed of a [2]triangulene (phenalenyl) and a [3]triangulene, as shown in Fig. 1a, are uncompensated ferrimagnetic insulators with spin-split bands[41] (see Fig. 1b,c). In this system, the [3]triangulene carries spin $S = 1$, while the [2]triangulene carries $S = 1/2$. The resulting band structure is highly unconventional: in the majority (minority) spin channel, shown in red (blue), a flat band merges with a dispersive band at the Γ point, forming a singular flat band that is fully occupied (empty). This flat band originates from a zero mode localized on the [3]triangulene molecule.

In order to make this structure conducting, we explore the addition of a substitutional nitrogen atom into the central carbon site of the [3]triangulene. This introduces an additional minority-spin electron, thereby reducing the magnetic moment of the [3]triangulene, promoting compensation of the total magnetization within the unit cell, and shifting the Fermi level into the conduction band. Both density functional theory calculations, performed using Quantum Espresso at the generalized gradient approximation level with PBE functionals[42–50], and mean-field Hubbard model calculations confirm this scenario. The resulting structure simultaneously exhibits three key features: a vanishing total magnetic moment (Fig. 1d), a Fermi energy located immediately be-

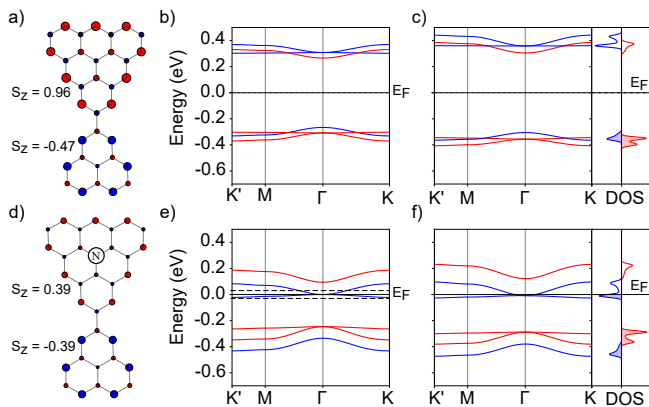


FIG. 1. DFT computed magnetic profiles, electronic band-structure and DOS (eV^{-1}) for the [2,3]triangulene a),b),c), and for the [2,A3]triangulene d),e),f). Spin up (down) is represented in red (blue) in the bandstructures computed via MFH b),e) and for the DFT magnetic profiles, bandstructures and DOS c),f). Solid line at 0 energy represents the Fermi level (E_F). Horizontal dashed lines in e), located at $\pm 25\text{meV}$, represent the values of the scanned energies used for computing LDOS.

low the singular flat band at the top of a dispersive band (Fig. 1e,f), and a very large density of states at the Fermi level that is fully spin polarized.

Our calculations for the resulting [2,A3]triangulene crystal confirm that the ground state retains the antiferromagnetic coupling between individual triangulenes, which is already present in the undoped crystal (Fig. 1a) due to intermolecular exchange interactions. Room-temperature stability is ensured, as the antiferromagnetic solution is approximately 59 meV lower in energy than the ferromagnetic one. Consequently, the [2,A3]triangulene crystal exhibits a total net spin of $S_z = 0$ in its ground state and thus realizes a fully compensated ferrimagnet.

We have verified that doping the central site with phosphorus or boron, instead of N, produces very similar results (see Fig. 5). Doping with a heavier atom such as P is equivalent to N substitution, as it introduces an extra electron into the system, shifting the Fermi level upward toward the Dirac point. Interestingly, using B instead of N or P, also leads to a half-metallic, fully compensated ferrimagnet. In this case, B removes an electron, lowering the Fermi level toward the Dirac point of the spin-up channel. In both cases, the Fermi level lies in close proximity to the flat bands, and the antiferromagnetic configuration remains the ground state. This configuration is energetically favored over the ferromagnetic one by approximately 81 meV for the P-doped system and 46 meV for the B-doped system, ensuring stability at room temperature. Together, these results reinforce those obtained for the [2,A3]triangulene crystal and demonstrate the robustness of our proposed strategy for realizing half-

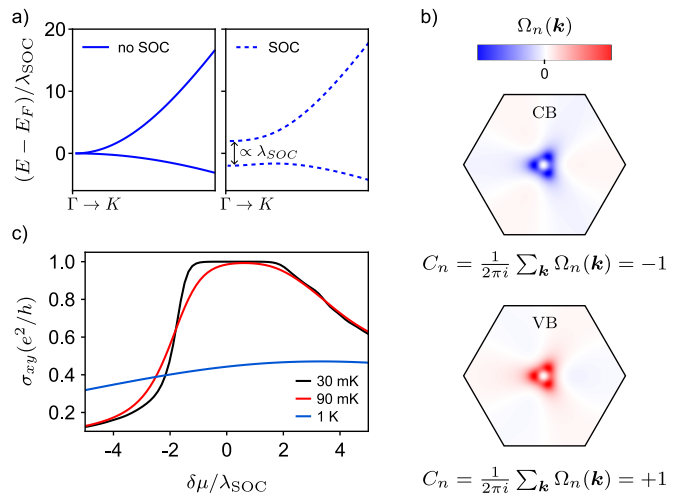


FIG. 2. a) Gap opening at the Γ point in the presence of intrinsic SOC. The size of the gap is proportional to the strength of SOC i.e. λ_{SOC} . b) Berry curvature, $\Omega_n(\mathbf{k})$, in the first Brillouin zone for the the valence band (VB) and conduction band (CB). c) Zero frequency Hall conductivity, as a function of the chemical potential detuning, $\delta\mu = \mu - E_F$, at three different temperatures. A value of $\lambda_{\text{SOC}} = 45\mu\text{eV}$ was used in the simulations.

metallic fully compensated ferrimagnets.

Having engineered the location of the Fermi level, we now discuss a remarkable property which arises from it: a finite Anomalous Hall Effect (AHE) despite the vanishing net magnetization in the crystal's unit-cell. The system we present complements recent studies on altermagnets and non-coplanar antiferromagnetic phases which also show finite AHE [51].

By analogy with the px-py honeycomb model [52], that also features singular flat bands at the Γ point, we expect that the presence of spin-orbit coupling (SOC) will open up a small gap at the Γ point [53], thus lifting the degeneracy between the dispersive and the nearly-flat bands. To capture this, we introduce a Kane-Mele [54, 55] intrinsic SOC term in the model Hamiltonian:

$$H_{\text{KM}} = i\lambda_{\text{SOC}} \sum_{\langle\langle i,j \rangle\rangle} \sum_{\sigma} \sigma \nu_{ij} c_{i,\sigma}^{\dagger} c_{j,\sigma} + \text{h.c.} \quad (1)$$

where λ_{SOC} quantifies the strength of intrinsic SOC ($\lambda_{\text{SOC}} = 45\mu\text{eV}$ in what follows), the first sum runs over second neighbors sites (i, j), the second over the spin component $\sigma = \uparrow, \downarrow$ and $\nu_{ij} = \pm 1 = \sigma \text{sign}[\hat{z} \cdot (\mathbf{r}_i \times \mathbf{r}_j)]$, depending on whether the electron makes a left (right) turn to go from site i at \mathbf{r}_i to site j at \mathbf{r}_j .

In Fig. 2a we show that, as expected, in the presence of SOC a small gap opens at the Γ point, with a magnitude proportional to λ_{SOC} . In this gapped phase the system becomes a topologically non-trivial Chern insulator. The bands around the Fermi level carry a finite Chern number [56, 57], with $C_n = +1$ for the valence band (VB) and $C_n = -1$ for the conduction band (CB), as depicted

in Fig. 2b. As λ_{SOC} decreases, the hot-spots of Berry curvature [57, 58], $\Omega_n(\mathbf{k})$, seen in Fig. 2b, approach the Γ point and perfectly cancel out in the $\lambda_{\text{SOC}} \rightarrow 0$ limit, when the two bands touch, returning the system to a trivial state.

A direct consequence of the finite Berry curvature is a finite value of the intrinsic Hall conductivity, σ_{xy} , defined as [51, 56, 57]:

$$\sigma_{xy} = -\frac{e^2}{2\pi h} \sum_{n,\mathbf{k}} \Omega_n(\mathbf{k}) f(E_n(\mathbf{k}), \mu, T), \quad (2)$$

where the sum over n runs over all bands of the system, \mathbf{k} is in the first Brillouin zone and $f(E_n(\mathbf{k}), \mu, T)$ is the Fermi-Dirac distribution for a state with energy $E_n(\mathbf{k})$, chemical potential μ and temperature T .

In Fig. 2c we show the intrinsic Hall conductivity, as given in Eq. (2), as a function of the chemical potential detuning, $\delta\mu = \mu - E_F$ at three different temperatures. At the lowest temperature, $T = 30\text{mK}$, we find a quantized Hall conductivity when $\delta\mu$ is small. In such a limit, the bands below the chemical potential are fully occupied, and the ones above it are fully empty; this reduces Eq. (2) to a sum over Chern numbers. We stress that this sum is only finite due to the carefully engineered location of E_F , and it would vanish in the undoped case. As $|\delta\mu|$ keeps increasing, μ eventually penetrates the VB or the CB bands and σ_{xy} stops being quantized as bands become partially filled. Repeating the same analysis for higher temperatures, a similar behavior is found, but the region where σ_{xy} is quantized decreases (and may even disappear), due to thermal occupation of high energy bands. This thermal occupation leads to a partial cancellation of the Berry curvatures of the VB and CB, taking σ_{xy} away from e^2/h , as we see in the simulation with $T = 1\text{K}$. Increasing λ_{SOC} , which could be achieved through doping with heavier atoms, for example, would increase the gap between VB and CB, leading to a wider energy window and larger temperature range where a quantized σ_{xy} could be measured. In Ref. [59], a Hall conductivity as small as $\sigma_{xy} = 0.2e^2/h$ was measured at $T = 30\text{mK}$, showing that it should be possible to probe the AHE in the system presently discussed.

A half-metallic fully compensated ferrimagnet is also peculiar from the point of view of its spin excitations. The metallic character of the electronic structure suggests strong electron-magnon coupling, which provides means of manipulating the magnetic state electrically but, on the other hand, may significantly reduce magnon lifetime through Landau damping [60–63]. The Néel-type magnetic ordering implies that magnons come in two flavors, distinguished by their $S^z = \pm 1$ quantum number. However, in sharp contrast to antiferromagnets, due to the spin polarization of the electronic bands $S^z = \pm 1$ magnons will have different energies, which depend on the the electronic bands in a non-trivial way. To ex-

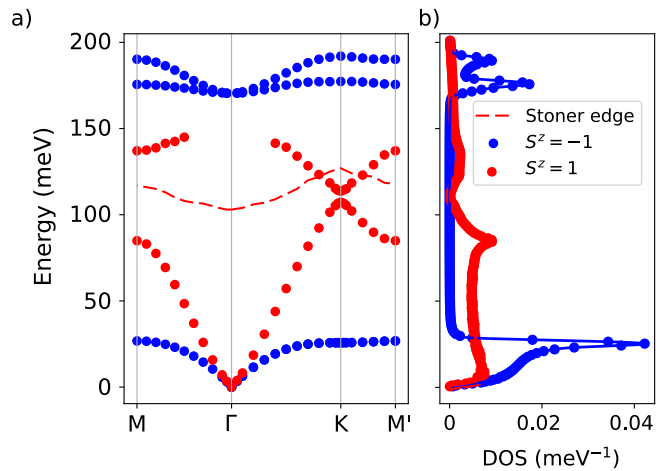


FIG. 3. a) Magnon energies for selected wave vectors extracted from the fermionic model, for the two magnon flavors $S^z = -1$ (blue) and $S^z = 1$ (red). The red dashed line marks the lower energy boundary of the $S^z = 1$ Stoner continuum. Notice the large magnon energies at the edges of the BZ, compatible with the large exchange estimated from the DFT calculation. b) Total magnon density of states for $S^z = -1$ (blue) and $S^z = 1$ (red). The solid lines are guides to the eye.

plore those properties we calculated the magnon spectrum, which is associated with the transverse components of the dynamic spin susceptibility tensor $\chi^\perp(\omega, \vec{q})$, within the random phase approximation (RPA) [60, 63, 64]. Magnon energies $\hbar\omega$ for a fixed wave vector \vec{q} are associated with the positions of the peaks of $-\text{Im}\chi^\perp(\omega, \vec{q})$ as ω is scanned. A dispersion relation for magnons along high symmetry lines in the Brillouin zone is shown in Fig. 7a. We find two magnon branches with distinct energies for each wave vector, corresponding to $S^z = \pm 1$. The modes are degenerate only at the Γ point (the Goldstone modes). The energy differences between the two modes are much larger than those found in altermagnets, for instance [63]. This can be qualitatively understood in terms of the large spin polarization of the electronic bands, see Fig. 1.

The two lowest energy branches in Fig. 7a correspond to modes in which the whole magnetization of each tri-angulene behave as a single, monolithic, spin (see supplementary material for a detailed discussion). This system also has higher energy $S^z = -1$ magnons that correspond to “internal” excitation modes of the individual aza-triangulene (the blue circles in the energy range of 150-200 meV). We had already encountered this kind of magnons in a half-metallic ferromagnetic system [62]. Here, however, the internal modes have energy below the edge of the Stoner continuum with $S^z = -1$ (~ 250 meV), which protects them from Landau damping. Finally, we also find a second branch of $S^z = 1$ magnons, with energies in the range 110-150 meV. These, however, overlap with the $S^z = 1$ Stoner continuum ex-

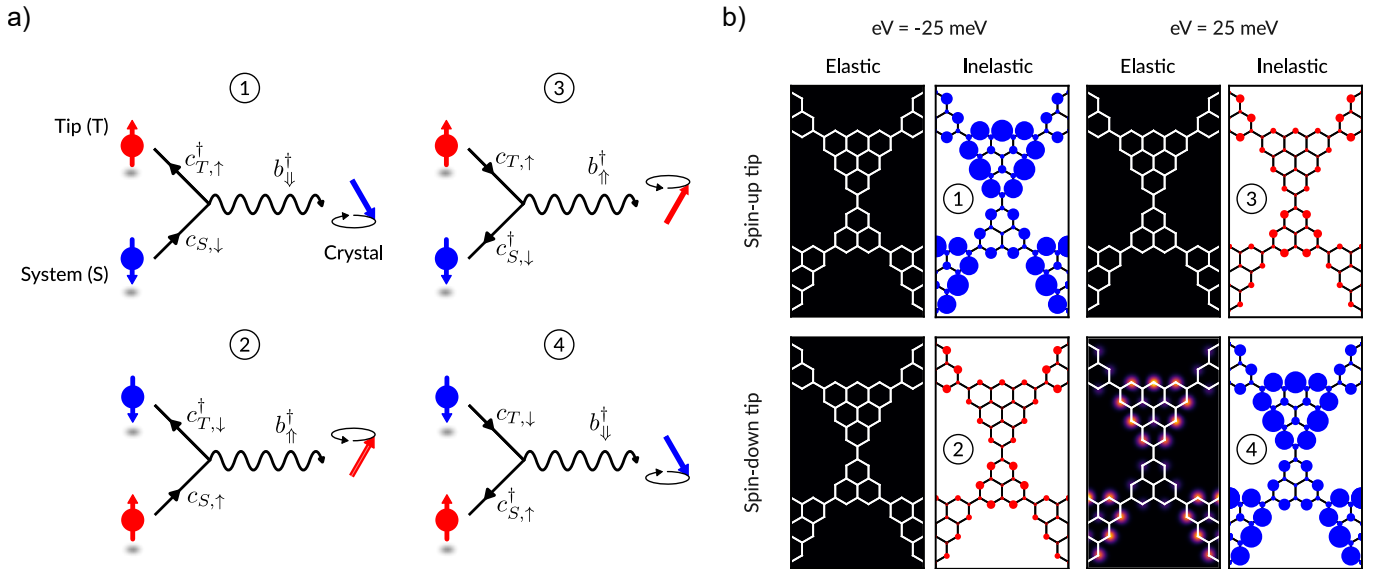


FIG. 4. **Detecting magnons with inelastic scanning tunneling spectroscopy.** The left panel a) shows schematic depictions of the inelastic tunneling processes that can lead to a feature associated with the emission of a magnon in the differential conductance of an ISTS experiment. The right panel b) shows local electron (elastic) and magnon (inelastic) local density of states maps for two values of the tip-sample bias: at $eV = -25$ meV elastic tunneling from the triangulene crystal is suppressed for both spin polarizations of the tip due to the absence of available electronic states; inelastic tunneling is possible by creating a magnon of either $S^z = \pm 1$. At $eV = 25$ meV, elastic tunneling is suppressed for tip polarization parallel to that of the individual aza-triangulene because the electronic band close to the Fermi level is polarized in the opposite direction. Inelastic tunneling is possible for both spin polarizations of the tip, each by exciting a magnon with the same energy polarization as the tip.

cept for a small pocket around the K point in the Brillouin zone. The missing energy points in the region around the Γ point correspond to overdamped $S^z = 1$ magnons. This analysis highlights the fact that it is impossible to describe the spin dynamics of this material based on spin-only models. Doping one of the triangulenes with nitrogen brings orbital degrees of freedom into play, which drastically affect the spin dynamics.

A metallic magnetic system in which most magnon modes live below the Stoner continuum is very unusual. This fact, as discussed previously, protects the magnons from Landau damping, thus blocking the main channel for magnon decay in metallic magnets. The remaining sources of magnon damping are either magnon-magnon interactions, which are expected to contribute little at low temperatures, and spin-orbit coupling mediated decay, which is negligible in carbon-based materials. Thus, this material sits at the sweet spot where magnons can be created electrically but are extremely long-lived, making it a prime candidate for use in magnonic devices [65].

We now address the question of how to probe the magnetic excitations of the compensated ferrimagnet using inelastic scanning tunneling spectroscopy (ISTS). The discussion is based on the Tersoff-Hamman approximation [66] for the differential conductance in a scanning

tunneling microscope,

$$\frac{dI}{dV} \propto n_{\text{tip}}^{\uparrow} n_{\text{sample}}^{\uparrow}(E_F + eV) + n_{\text{tip}}^{\downarrow} n_{\text{sample}}^{\downarrow}(E_F + eV), \quad (3)$$

where n^{σ} is the density of states for spin channel σ and V is the tip-sample bias voltage. The spin excitations of the sample renormalize its density of states [67], leading to signatures in the dI/dV spectrum which are roughly proportional to the density of magnon states, shown in Fig. 7b. To simplify the discussion, the tunneling current can be thought of as having two contributions for a given tip-sample bias V : one elastic, coming from tunneling to/from electronic states of the sample with energy $E_F \pm e|V|$, and one inelastic, coming from tunneling aided by an excitation with energy $\hbar\omega \geq |V|$. In our crystal there are no electronic states with energies between $\sim E_F - 25$ meV and $\sim E_F + 25$ meV. Thus, the only tunneling processes allowed for -250 meV $\lesssim eV \lesssim -25$ meV are those mediated by the emission of a magnon. Within that range there is a finite density of magnon states for $S^z = 1$ magnons, which would be clearly visible in conventional ISTS experiments. Moreover, if a spin-polarized tip is available, the energy range over which the tunneling is dominated by the inelastic contribution can be extended to -250 meV $\lesssim eV \lesssim 0$. Starting from a Néel state in which the individual aza-triangulenes are polarized \uparrow , the electronic states around E_F have spin \downarrow . If the tip is \uparrow -polarized, at negative bias ($V < 0$) there is

no elastic contribution to the tunneling. There is, however, a contribution coming from an inelastic process in which an electron in the crystal, initially with spin \downarrow , emits a magnon with $S^z = -1$ and tunnels to the tip with spin \uparrow . The intensity of the inelastic tunneling current is roughly proportional to the density of states of the excitation, which is shown in Fig. 7b (blue symbols). Thus, the magnon signature should be clearly seen in ISTS experiments at negative bias, with or without spin-polarized tips.

To further illustrate how magnons could be detected by ISTS, we analyze the local density of states for electrons and magnons in Fig. 4. We also provide schematic representations of the possible inelastic processes in the presence of a spin-polarized tip. The two tip-sample bias values $eV = \pm 25$ meV were chosen to maximize the contribution of the inelastic signal. The $S^z = -1$ magnon DOS has a sharp peak at 25 meV, due to their almost flat dispersion curve around that energy. On the other hand, elastic tunneling at $eV = -25$ meV is suppressed for both spin polarizations of the tip, since the electron DOS at $E_F - 25$ meV is zero (see Fig. 1). Finally, elastic tunneling at $eV = 25$ meV is suppressed for tip polarization parallel to the polarization of the individual azatriangulene, since the electron DOS at $E_F + 25$ meV is zero for that polarization.

In conclusion, we have demonstrated that molecular crystals formed by combining doped and undoped nanographenes can simultaneously realize half-metallicity and fully compensated ferrimagnetism — two properties long sought in condensed matter physics but rarely found together, and never before in a purely organic, pi-electron system. The nitrogen-substituted [2,A3]triangulene crystal emerges as a singular platform: its Fermi level sits at a spin-polarized flat band, its magnetic order is robust well above room temperature, and its vanishing net magnetization eliminates the stray fields that plague conventional spintronic devices. Beyond the half-metallic ground state, the system hosts a quantized anomalous Hall effect driven by Berry curvature concentrated near the Γ point, and a magnon spectrum in which most modes are shielded from Landau damping — a combination that is almost paradoxical in a metal. The accessibility of these excitations to inelastic scanning tunneling spectroscopy, and the robustness of the phenomenology to different dopants, suggests that experimental realization is within reach using existing on-surface synthesis techniques. Taken together, these results establish triangulene crystals as a compelling new frontier for carbon-based spintronics and magnonics, and open a design pathway toward functional organic quantum materials engineered atom by atom.

J.F.-R., J.C.G.H., J.P. and A.T.C. acknowledge financial support from FCT (Grant No. PTDC/FIS-MAC/2045/2021), SNF Sinergia (Grant Pimag, CRSII5.205987) J.F.-R. acknowledges financial fund-

ing from Generalitat Valenciana (Prometeo2021/017 and MFA/2022/045) and MICIN-Spain (Grants No. PID2022-141712NB-C22) The authors thankfully acknowledge RES resources provided by Barcelona Supercomputing Centre in MareNostrum 5 to FI-2025-3-0039. The authors acknowledge the use of computer time at MareNostrum 5 (Barcelona Supercomputing Centre) provided through FCT grant 2025.00090.CPCA.A2.

* On permanent leave from Departamento de Física Aplicada, Universidad de Alicante, 03690 San Vicente del Raspeig, Spain.

† jan.phillips@inl.int

- [1] L.-D. Yuan, Z. Wang, J.-W. Luo, E. I. Rashba, and A. Zunger, *Phys. Rev. B* **102**, 014422 (2020).
- [2] S. Hayami, Y. Yanagi, and H. Kusunose, *Phys. Rev. B* **102**, 144441 (2020).
- [3] L.-D. Yuan, Z. Wang, J.-W. Luo, and A. Zunger, *Phys. Rev. Mater.* **5**, 014409 (2021).
- [4] J. Dong, K. Wu, M. Zhu, F. Zheng, X. Li, and J. Zhang, *Phys. Rev. B* **112**, 024425 (2025).
- [5] T. Jungwirth, X. Marti, P. Wadley, and J. Wunderlich, *Nature nanotechnology* **11**, 231 (2016).
- [6] J. Dong, X. Li, G. Gurung, M. Zhu, P. Zhang, F. Zheng, E. Y. Tsybal, and J. Zhang, *Phys. Rev. Lett.* **128**, 197201 (2022).
- [7] L. Šmejkal, A. B. Hellenes, R. González-Hernández, J. Sinova, and T. Jungwirth, *Phys. Rev. X* **12**, 011028 (2022).
- [8] L. Šmejkal, J. Sinova, and T. Jungwirth, *Phys. Rev. X* **12**, 031042 (2022).
- [9] L. Šmejkal, J. Sinova, and T. Jungwirth, *Phys. Rev. X* **12**, 040501 (2022).
- [10] R. A. de Groot, F. M. Mueller, P. G. v. Engen, and K. H. J. Buschow, *Phys. Rev. Lett.* **50**, 2024 (1983).
- [11] R. A. de Groot, *Physica B: Condensed Matter* **172**, 45 (1991).
- [12] W. E. Pickett, *Phys. Rev. B* **57**, 10613 (1998).
- [13] I. Galanakis, P. H. Dederichs, and N. Papanikolaou, *Phys. Rev. B* **66**, 174429 (2002).
- [14] J. Železný, P. Wadley, K. Olejník, A. Hoffmann, and H. Ohno, *Nature Physics* **14**, 220 (2018).
- [15] J. Finley and L. Liu, *Applied Physics Letters* **116**, 110501 (2020).
- [16] Y. Zhou and F. Liu, *Nano Letters* **21**, 230 (2020).
- [17] S. Mishra, D. Beyer, K. Eimre, J. Liu, R. Berger, O. Gröning, C. A. Pignedoli, K. Müllen, R. Fasel, X. Feng, *et al.*, *Journal of the American Chemical Society* **141**, 10621 (2019).
- [18] J. Li, S. Sanz, J. Castro-Esteban, M. Vilas-Varela, N. Friedrich, T. Frederiksen, D. Peña, and J. I. Pascual, *Physical Review Letters* **124**, 177201 (2020).
- [19] S. Mishra, D. Beyer, K. Eimre, R. Ortiz, J. Fernández-Rossier, R. Berger, O. Gröning, C. A. Pignedoli, R. Fasel, X. Feng, and P. Ruffieux, *Angewandte Chemie* **132**, 12139 (2020).
- [20] S. Mishra, D. Beyer, K. Eimre, S. Kezilebieke, R. Berger, O. Gröning, C. A. Pignedoli, K. Müllen, P. Liljeroth, P. Ruffieux, *et al.*, *Nature nanotechnology* **15**, 22 (2020).

- [21] R. Ortiz and J. Fernández-Rossier, *Progress in Surface Science* **95**, 100595 (2020).
- [22] E. Turco, A. Bernhardt, N. Krane, L. Valenta, R. Fasel, M. Jurićček, and P. Ruffieux, *JACS Au* **3**, 1358 (2023).
- [23] S. Mishra, X. Yao, Q. Chen, K. Eimre, O. Gröning, R. Ortiz, M. Di Giovannantonio, J. C. Sancho-García, J. Fernández-Rossier, C. A. Pignedoli, *et al.*, *Nature chemistry* **13**, 581 (2021).
- [24] S. Mishra, G. Catarina, F. Wu, R. Ortiz, D. Jacob, K. Eimre, J. Ma, C. A. Pignedoli, X. Feng, P. Ruffieux, *et al.*, *Nature* **598**, 287 (2021).
- [25] J. Hieulle, S. Castro, N. Friedrich, A. Vegliante, F. R. Lara, S. Sanz, D. Rey, M. Corso, T. Frederiksen, J. I. Pascual, *et al.*, *Angewandte Chemie International Edition* **60**, 25224 (2021).
- [26] T. Wang, A. Berdonces-Layunta, N. Friedrich, M. Vilas-Varela, J. P. Calupitan, J. I. Pascual, D. Peña, D. Casanova, M. Corso, and D. G. de Oteyza, *Journal of the American Chemical Society* **144**, 4522 (2022).
- [27] S. Cheng, Z. Xue, C. Li, Y. Liu, L. Xiang, Y. Ke, K. Yan, S. Wang, and P. Yu, *Nature communications* **13**, 1705 (2022).
- [28] H. Yu and T. Heine, arXiv preprint arXiv:2508.17264 (2025).
- [29] H. Yu and T. Heine, *J. Am. Chem. Soc.* **145**, 19303 (2023).
- [30] H. Yu, Y. Jing, and T. Heine, *Accounts of Chemical Research* **58**, 61 (2025), pMID: 39656556, <https://doi.org/10.1021/acs.accounts.4c00557>.
- [31] K. N. Anindya and A. Rochefort, *Carbon Trends* **7**, 100170 (2022).
- [32] R. Ortiz, K. Strutyński, and M. Melle-Franco, *2D Materials* **13**, 015023 (2026).
- [33] J. Cai, P. Ruffieux, R. Jaafar, M. Bieri, T. Braun, S. Blankenburg, M. Muoth, A. P. Seitsonen, M. Saleh, X. Feng, *et al.*, *Nature* **466**, 470 (2010).
- [34] C. Moreno, M. Vilas-Varela, B. Kretz, A. Garcia-Lekue, M. V. Costache, M. Paradinas, M. Panighel, G. Ceballos, S. O. Valenzuela, D. Peña, and A. Mugarza, *Science* **360**, 199 (2018), <https://www.science.org/doi/pdf/10.1126/science.aar2009>.
- [35] S. Song, J. Su, M. Telychko, J. Li, G. Li, Y. Li, C. Su, J. Wu, and J. Lu, *Chem. Soc. Rev.* **50**, 3238 (2021).
- [36] N. Pavliček, A. Mistry, Z. Majzik, N. Moll, G. Meyer, D. J. Fox, and L. Gross, *Nature Nanotechnology* **12**, 308 (2017).
- [37] J. Su, M. Telychko, P. Hu, G. Macam, P. Mutombo, H. Zhang, Y. Bao, F. Cheng, Z.-Q. Huang, Z. Qiu, *et al.*, *Science advances* **5**, eaav7717 (2019).
- [38] S. Mishra, K. Xu, K. Eimre, H. Komber, J. Ma, C. A. Pignedoli, R. Fasel, X. Feng, and P. Ruffieux, *Nanoscale* **13**, 1624 (2021).
- [39] A. Delgado, C. Dusold, J. Jiang, A. Cronin, S. G. Louie, and F. R. Fischer, Evidence for excitonic insulator ground state in triangulene Kagome lattice (2023), arXiv:2301.06171.
- [40] R. Pawlak, K. N. Anindya, O. Chahib, J.-C. Liu, P. Hiret, L. Marot, V. Luzet, F. Palmino, F. Chérioux, A. Rochefort, and E. Meyer, *ACS Nano* **19**, 4768 (2025), pMID: 39793973, <https://doi.org/10.1021/acs.nano.4c15519>.
- [41] G. Catarina, J. C. G. Henriques, A. Molina-Sánchez, A. T. Costa, and J. Fernández-Rossier, *Phys. Rev. Res.* **5**, 043226 (2023).
- [42] P. Giannozzi, O. Andreussi, T. Brumme, O. Bunau, M. B. Nardelli, M. Calandra, R. Car, C. Cavazzoni, D. Ceresoli, M. Cococcioni, N. Colonna, I. Carnimeo, A. D. Corso, S. de Gironcoli, P. Delugas, R. A. D. Jr, A. Ferretti, A. Floris, G. Fratesi, G. Fugallo, R. Gebauer, U. Gerstmann, F. Giustino, T. Gorni, J. Jia, M. Kawamura, H.-Y. Ko, A. Kokalj, E. Küçükbenli, M. Lazzeri, M. Marsili, N. Marzari, F. Mauri, N. L. Nguyen, H.-V. Nguyen, A. O. de-la Roza, L. Paulatto, S. Poncé, D. Rocca, R. Sabatini, B. Santra, M. Schlipf, A. P. Seitsonen, A. Smogunov, I. Timrov, T. Thonhauser, P. Umari, N. Vast, X. Wu, and S. Baroni, *Journal of Physics: Condensed Matter* **29**, 465901 (2017).
- [43] P. Giannozzi, S. Baroni, N. Bonini, M. Calandra, R. Car, C. Cavazzoni, D. Ceresoli, G. L. Chiarotti, M. Cococcioni, I. Dabo, A. Dal Corso, S. de Gironcoli, S. Fabris, G. Fratesi, R. Gebauer, U. Gerstmann, C. Gougoussis, A. Kokalj, M. Lazzeri, L. Martin-Samos, N. Marzari, F. Mauri, R. Mazzarello, S. Paolini, A. Pasquarello, L. Paulatto, C. Sbraccia, S. Scandolo, G. Sclauzero, A. P. Seitsonen, A. Smogunov, P. Umari, and R. M. Wentzcovitch, *Journal of Physics: Condensed Matter* **21**, 395502 (19pp) (2009).
- [44] P. Giannozzi, O. Baseggio, P. Bonfà, D. Brunato, R. Car, I. Carnimeo, C. Cavazzoni, S. de Gironcoli, P. Delugas, F. Ferrari Ruffino, A. Ferretti, N. Marzari, I. Timrov, A. Urru, and S. Baroni, *The Journal of Chemical Physics* **152**, 154105 (2020), <https://doi.org/10.1063/5.0005082>.
- [45] D. R. Hamann, M. Schlüter, and C. Chiang, *Phys. Rev. Lett.* **43**, 1494 (1979).
- [46] N. Troullier and J. L. Martins, *Phys. Rev. B* **43**, 1993 (1991).
- [47] M. van Setten, M. Giantomassi, E. Bousquet, M. Verstraete, D. Hamann, X. Gonze, and G.-M. Rignanese, *Computer Physics Communications* **226**, 39–54 (2018).
- [48] D. R. Hamann, *Phys. Rev. B* **88**, 085117 (2013).
- [49] K. F. Garrity, J. W. Bennett, K. M. Rabe, and D. Vanderbilt, *Computational Materials Science* **81**, 446 (2014).
- [50] K. Lejaeghere, G. Bihlmayer, T. Björkman, P. Blaha, S. Blügel, V. Blum, D. Caliste, I. E. Castelli, S. J. Clark, A. D. Corso, S. de Gironcoli, T. Deutsch, J. K. Dewhurst, I. D. Marco, C. Draxl, M. Dulak, O. Eriksson, J. A. Flores-Livas, K. F. Garrity, L. Genovese, P. Giannozzi, M. Giantomassi, S. Goedecker, X. Gonze, O. Grånäs, E. K. U. Gross, A. Gulans, F. Gygi, D. R. Hamann, P. J. Hasnip, N. A. W. Holzwarth, D. Iuşan, D. B. Jochym, F. Jollet, D. Jones, G. Kresse, K. Koepnik, E. Küçükbenli, Y. O. Kvashnin, I. L. M. Locht, S. Lubeck, M. Marsman, N. Marzari, U. Nitzsche, L. Nordström, T. Ozaki, L. Paulatto, C. J. Pickard, W. Poelmans, M. I. J. Probert, K. Refson, M. Richter, G.-M. Rignanese, S. Saha, M. Scheffler, M. Schlipf, K. Schwarz, S. Sharma, F. Tavazza, P. Thunström, A. Tkatchenko, M. Torrent, D. Vanderbilt, M. J. van Setten, V. V. Speybroeck, J. M. Wills, J. R. Yates, G.-X. Zhang, and S. Cottenier, *Science* **351**, aad3000 (2016), <https://www.science.org/doi/pdf/10.1126/science.aad3000>.
- [51] L. Šmejkal, A. H. MacDonald, J. Sinova, S. Nakatsuji, and T. Jungwirth, *Nature Reviews Materials* **7**, 482 (2022).
- [52] C. Wu, D. Bergman, L. Balents, and S. D. Sarma, *Physical review letters* **99**, 070401 (2007).
- [53] G.-F. Zhang, Y. Li, and C. Wu, *Physical Review B* **90**, 075114 (2014).

- [54] C. L. Kane and E. J. Mele, *Physical review letters* **95**, 226801 (2005).
- [55] H. Min, J. Hill, N. A. Sinitsyn, B. Sahu, L. Kleinman, and A. H. MacDonald, *Physical Review B—Condensed Matter and Materials Physics* **74**, 165310 (2006).
- [56] T. Fukui, Y. Hatsugai, and H. Suzuki, *Journal of the Physical Society of Japan* **74**, 1674 (2005).
- [57] M. Z. Hasan and C. L. Kane, *Reviews of modern physics* **82**, 3045 (2010).
- [58] M. V. Berry, *Proceedings of the Royal Society of London. A. Mathematical and Physical Sciences* **392**, 45 (1984).
- [59] C.-Z. Chang, J. Zhang, X. Feng, J. Shen, Z. Zhang, M. Guo, K. Li, Y. Ou, P. Wei, L.-L. Wang, Z.-Q. Ji, Y. Feng, S. Ji, X. Chen, J. Jia, X. Dai, Z. Fang, S.-C. Zhang, K. He, Y. Wang, L. Lu, X.-C. Ma, and Q.-K. Xue, *Science* **340**, 167 (2013).
- [60] L. H. M. Barbosa, R. B. Muniz, A. T. Costa, and J. Mathon, *Phys. Rev. B* **63**, 174401 (2001).
- [61] M. Costa, N. M. R. Peres, J. Fernández-Rossier, and A. T. Costa, *Phys. Rev. B* **102**, 014450 (2020).
- [62] J. Henriques, D. Jacob, A. Molina-Sánchez, G. Catarina, A. T. Costa, and J. Fernández-Rossier, *Nano Letters* **24**, 12928 (2024), pMID: 39374927, <https://doi.org/10.1021/acs.nanolett.4c03416>.
- [63] A. T. Costa, J. C. G. Henriques, and J. Fernández-Rossier, *SciPost Phys.* **18**, 125 (2025).
- [64] J. C. G. Henriques and J. Fernández-Rossier, *Phys. Rev. B* **108**, 155423 (2023).
- [65] A. Fert, R. Ramesh, V. Garcia, F. Casanova, and M. Bibes, *Rev. Mod. Phys.* **96**, 015005 (2024).
- [66] J. Tersoff and D. R. Hamann, *Phys. Rev. B* **31**, 805 (1985).
- [67] B. Schweefinghaus, M. dos Santos Dias, A. T. Costa, and S. Lounis, *Phys. Rev. B* **89**, 235439 (2014).
- [68] D. Jacob and J. Fernández-Rossier, *Physical Review B* **106**, 205405 (2022).

SUPPLEMENTARY MATERIAL

DFT

Density Functional Theory (DFT) results were obtained using the QUANTUM ESPRESSO package [42–44]. We used norm-conserving pseudopotentials [45–50]. The plane-wave energy cutoff was converged to a value of 70 Ry for the wave functions and 280 Ry for the charge density. The Brillouin zone integrals for the relaxations were performed in a converged $15 \times 15 \times 1$ k-point grid with a gaussian smearing of 0.001 Ry. In-plane lattice parameters and internal atomic positions were relaxed for every doped structure (Fig 5). The crystals include a converged 9 Å vacuum for the z-axis to avoid inter-molecular interactions.

The computed LDOS in Fig. 6 shows that the flat band at the Fermi level comes mainly from states of the [3]triangulene. When scanning the band 0.1 eV higher in energy, we observe the contribution from the [2]triangulene states start to appear. At 0.2 eV the [3]triangulene states disappear in the LDOS and the contribution

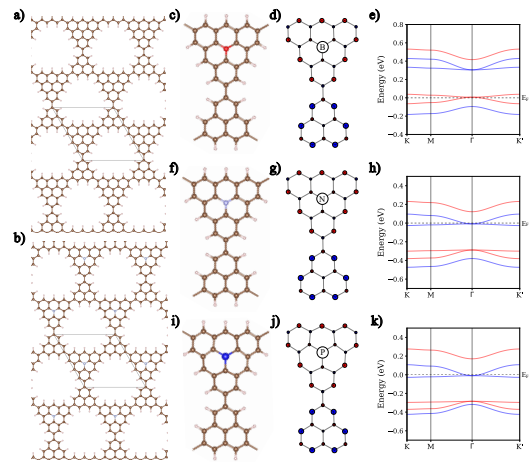


FIG. 5. Crystal structure for a) the undoped [2,3]triangulene and b) the doped triangulene. Brown atoms represent C atoms, light pink represent H atoms and the doped atom at the center of the [3]triangulene is represented in light blue. Different computed doped structures are represented, when doping with boron c),d),e), with nitrogen f),g),h) and with phosphorus i),j),k). Monomers for the different doped structures are shown c),f),i), together with their respective magnetic profiles d),g),j) and their corresponding bandstructures e),h),k). In the magnetic profiles and the bandstructures, red (blue) represents spin up (down). Fermi level is depicted with a dashed line in the bandstructure plots, and it becomes obvious that for every doped case it lies very close to a nearly flat band.

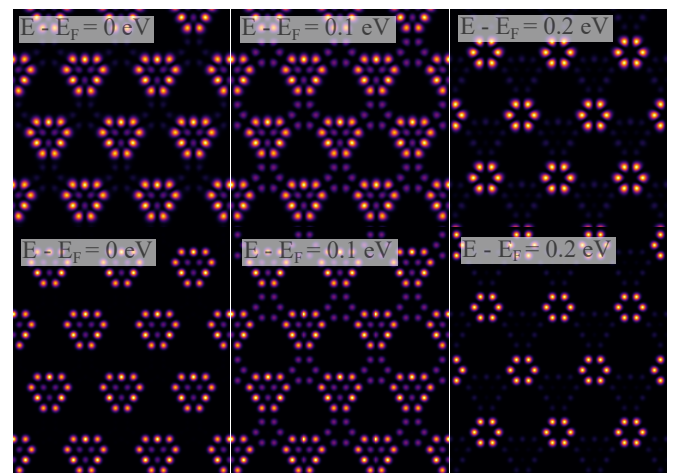


FIG. 6. Comparison of the computed LDOS using DFT (top row) and Mean-field Hubbard (bottom row). For every caption the energy at which the LDOS is computed is shown, referenced to the Fermi level.

is solely from the [2]triangulene. These statements are true for both DFT and MFH and is yet another example of the excellent agreement between them in this system.

MEAN-FIELD HUBBARD

The mean-field Hubbard (MFH) calculations were performed using the Hamiltonian $H = H_{TB} + H_U$ as a starting point. For the system studied in the main text, we consider the minimal model with first neighbour hopping, t , only. The corresponding tight-binding Hamiltonian is given by

$$H_{TB} = t \sum_{\langle i,j \rangle} \sum_{\sigma=\uparrow,\downarrow} c_{i\sigma}^\dagger c_{j\sigma} \quad (4)$$

where $c_{i\sigma}^\dagger$ denotes the annihilation (creation) operator of an electron with spin projection $\sigma = \uparrow, \downarrow$ at site i , and the sum runs over nearest neighbouring sites and spin index. This tight-binding model can be diagonalized exactly, and its eigenstates are termed molecular orbitals. In bipartite nanographenes, the sublattice imbalance enforces a certain number of zero modes. Due to their sublattice polarization, third neighbour hopping is usually included to allow the zero modes of different units to hybridize[68].

Then, a mean field decoupling of the Hubbard interaction term is introduced:

$$H_U \approx \sum_i U_i [n_{i\uparrow} \langle n_{i\downarrow} \rangle + \langle n_{i\uparrow} \rangle n_{i\downarrow} - \langle n_{i\uparrow} \rangle \langle n_{i\downarrow} \rangle] \quad (5)$$

Where $\langle n_{i\sigma} \rangle$ refers to the expectation value of the number operator on site i and spin σ , taken over the mean-field ground state. This ground state is determined iteratively in a self-consistent manner until convergence is reached.

MAGNON SPECTRUM

The energies and lifetimes of the magnons with $S^z = -1$ and $S^z = 1$ were obtained from the dynamic transverse spin susceptibilities, calculated within the random phase approximation (RPA),

$$\begin{aligned} \chi_{ll'}^{+-}(t) &\equiv -i\theta(t) \langle [S_l^+(t), S_{l'}^-(0)] \rangle, \\ \chi_{ll'}^{-+}(t) &\equiv -i\theta(t) \langle [S_l^-(t), S_{l'}^+(0)] \rangle, \end{aligned} \quad (6)$$

where $S_l^+ \equiv a_{l\uparrow}^\dagger a_{l\downarrow}$, $S_l^- \equiv a_{l\downarrow}^\dagger a_{l\uparrow}$, l is a site index, $\langle \cdot \rangle$ is a thermodynamic average and $\theta(t)$ is the Heaviside unit step function. The magnon spectral densities are defined as the imaginary part of the frequency-domain susceptibilities,

$$\chi_{ll'}^\perp(\omega) = \int_{-\infty}^{\infty} e^{i\omega t} \chi_{ll'}^\perp(t) dt, \quad (7)$$

where \perp stands for either $+-$ or $-+$. The RPA consists in decoupling the dynamics of the majority and minority spin electrons at the level of the equation of motion for the susceptibility or, equivalently, summing up the

ladder diagrams in the perturbation series to all orders. Both procedures result in the same final expression for the susceptibility [60],

$$\chi_{ll'}^\perp(\omega) = \tilde{\chi}_{ll'}^\perp(\omega) + \sum_m \tilde{\chi}_{lm}^\perp(\omega) U_m \chi_{ml'}^\perp(\omega), \quad (8)$$

where $\tilde{\chi}^\perp$ is the susceptibility defined in Eq. 6 calculated for the mean-field Hamiltonian (Eq. 5). In this work the site indices l, l' can be separated into a unit cell index (indicating the position of a triangulene dimer) and an atom index (indicating the position of an atom inside the unit cell). Due to translation symmetry in the unit cell index, it is possible to adopt a mixed wave-vector/atomic site representation in which the transverse susceptibility is a matrix in atomic site indices l , whose elements are functions of a two-dimensional wave vector \vec{q} . The RPA equation then becomes,

$$\chi_{ll'}^\perp(\omega; \vec{q}) = \tilde{\chi}_{ll'}^\perp(\omega; \vec{q}) + \sum_m \tilde{\chi}_{lm}^\perp(\omega; \vec{q}) U_m \chi_{ml'}^\perp(\omega; \vec{q}). \quad (9)$$

The mean-field susceptibilities $\tilde{\chi}_{ll'}^\perp(\omega; \vec{q})$ were calculated by numerical evaluation of the \vec{k} -space sums,

$$\tilde{\chi}_{lm}^{+-}(\omega; \vec{q}) = \sum_{\mu, \nu, \vec{k}} \frac{\phi_{l;\uparrow}^{(\mu)*}(\vec{k}) \phi_{m;\uparrow}^{(\mu)}(\vec{k}) \phi_{l;\downarrow}^{(\nu)}(\vec{k} + \vec{q}) \phi_{m;\downarrow}^{(\nu)*}(\vec{k} + \vec{q}) \{f[E_\mu^+(\vec{k})] - f[E_\nu^+(\vec{k} + \vec{q})]\}}{\omega + E_\mu^+(\vec{k}) - E_\nu^+(\vec{k} + \vec{q}) + i\eta}, \quad (10)$$

and an analogous expression for $\tilde{\chi}^{-+}$, with the spin indices reversed. Here η is a (small) regularization parameter, and

$$|\vec{k}; \mu; \sigma\rangle \equiv \sum_{l, \vec{R}} e^{i\vec{k} \cdot \vec{R}} \phi_{l;\sigma}^{(\mu)}(\vec{k}) |l; \vec{R}\rangle, \quad (11)$$

are the eigenstates of the mean-field Hamiltonian H_{MF}^σ for spin direction σ , with energies $E_\mu^\sigma(\vec{k})$, written in the basis of atomic-like states $|l; \vec{R}\rangle$ localized at atomic site l in unit cell \vec{R} . For the results presented in this work we adopted $\eta = 0.1$ meV and summed over 478800 \vec{k} points.

As shown in Fig. 3 of the main text (also reproduced here for ease of reference), the $S^z = 1$ magnon dispersion has two branches, that are commonly referred to as acoustic (low-energy, linearly vanishing at Γ) and optical (high-energy, usually an extreme at Γ). The energy points for the optical branch around the Γ -point are conspicuously missing from that plot. Here we address the reason for that absence, which is as follows. The acoustic branch has a well-defined signature with vanishing linewidth over the whole Brillouin zone. The optical branch, however, merges with the Stoner continuum around the Γ -point, and ceases to be identifiable as a true collective mode. In Fig. 7 we show the evolution of the $S^z = 1$ magnon spectral density along the $K - \Gamma$ direction by plotting $A^\gamma(\omega, \vec{q})$, where

$$A(\omega, \vec{q}) \equiv -\frac{1}{\pi} \text{Im} \sum_l \chi_{ll}^{-+}(\omega, \vec{q}), \quad (12)$$

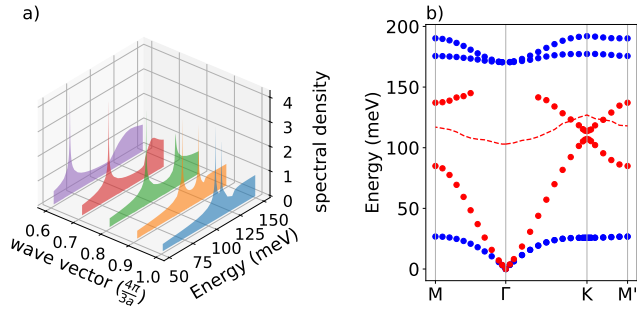


FIG. 7. a) Power-compressed spectral density $A^\gamma(\omega, \vec{q})$ as a function of magnon energy $\hbar\omega$ for selected wave vectors along $\Gamma-K$. As the wave vector departs from K (blue spectral density) the energy of the acoustic magnon (lower-energy peak) decreases, whereas that of the optical magnon (higher-energy peak) increases, eventually leading to the disappearance of the optical magnon peak into the Stoner continuum. b) Magnon energies for selected wave vectors extracted from the fermionic model, for the two magnon flavors $S^z = -1$ (blue) and $S^z = 1$ (red). The red dashed line marks the lower energy boundary of the $S^z = 1$ Stoner continuum.

$\chi_{ll}^{-+}(\omega, \vec{q})$ is the transverse spin susceptibility associated with $S^z = 1$ magnons, l are sites in the crystal's unit cell, and $\gamma = 0.2$ is a compression factor to help the visualization of the very sharp peaks in the spectral function. The optical mode starts as a well-defined collective excitation at the K -point, but as its energy increases it quickly approaches the Stoner continuum, merging with it and becoming overdamped at a point between 70% and 80% of the way from K to Γ .